Characterizing interference effects of vortex beams based on the Sagnac interferometer

Mairikena Aili, Xiao-Xiao Chen, Pan Liu, Jia-Zhi Yang, Xue Guo,
Jian Li, Zhe Meng, Qing-Yuan Wu, and An-Ning Zhang*
Center for Quantum Technology Research and Key Laboratory of Advanced Optoelectronic Quantum Architecture and Measurements, School of Physics, Beijing Institute of Technology, Haidian District, Beijing 100081, People's Republic of China

(Received 21 May 2022; accepted 12 August 2022; published 26 August 2022)

Orbital angular momentum (OAM) of photons has applications both in classical and quantum information due to its features of optical vortex and infinite dimensions. This paper studies the interference effects of optical vortex beams carrying mixed, conjugate, and single-mode OAM states based on the Sagnac interferometer with light sources of a laser and single photon. We compare our results with numerical simulations and show that the light intensity distribution and phase characteristics can directly characterize the absolute value of the topological charge (TC) carried by vortex beams. Furthermore, our scheme can also classify the photon with positive and negative signs of TC in the mixed mode OAM state by changing the relative phase. The results not only extend the manipulation methods for high-dimensional quantum states, but also lay a solid foundation for the application of vortex beams in a single-photon field.

DOI: 10.1103/PhysRevA.106.023715

I. INTRODUCTION

Over the past few decades, the exploration of quantum information has opened up profound prospects both for fundamental physics and technological applications. Specifically, quantum optics has enabled the implementation of a variety of quantum information protocols, such as the manipulation capability of quantum systems and quantum communication. However, in this context the standard information encoding based on the two-dimensional quantum space of photon spin angular momentum (SAM) brings great limitations to the high-dimensional quantum protocols. In 1992, the beam with orbital angular momentum (OAM) was discovered by Allen [1]. It was regarded as an ideal resource for high-dimensional quantum information protocols, allowing the implementation with a single photon of a higher-dimensional quantum space, or a "qudit" [2,3]. OAM is associated with vortex phase structure $e^{im\phi}$, where m is the topological charge (TC), is a characteristic value of OAM.

One remarkable characteristic of OAM is its orthogonality. The OAM beam with different TC can produce a high-dimensional state to achieve high capacity, multimode multiplexing and demultiplexing in optical communication [4,5] and micromanipulation [6]. When OAM is combined with SAM, it can produce high-dimensional entanglement or a product state to provide increased security and robustness [7,8] for quantum communications. Therefore, the OAM states measurement is key for all its practical applications. So far, various techniques were investigated for the OAM state measurement based on the interferometer, such as the Mach-Zehnder (MZ) interferometer [9–11], Fizeau interferometer [12], double-slit interferometer [13], multipoint or multipinhole interferometer [14], and self-reference interferometry [15,16]. However, the above interferometer techniques require higher stability and finer path matching of interferometers, which makes these techniques less practical. The Sagnac interferometer (SI) is a quite stable interferometer which has been used in OAM research. Slussarenko *et al.* sorted and detected the OAM components of spin-orbit states by the SI in 2010 [17]. In 2017, Wang *et al.* studied the manipulating method for OAM photon states in the single-path SI [18]. In the same year, Jabir *et al.* generated two-photon nonseparable states in the polarized SI [19]. In 2018, Xiao *et al.* detected the rotation-vibration signal of the light beam with different values of OAM in the polarized Sagnac interferometer [20]. Recently, Zhang *et al.* proposed an estimation protocol based on a SI using coherent-state carrying orbital angular momentum [21]. Most of these works used the Dove prism (DP) to manipulate OAM light. The DP always changes both the clockwise and anticlockwise paths of SI at the same time, which makes the OAM state complex and decreases the visibility of the SI in some works [18,22]. In addition, the previous experiment was confined to a single type of mode interference between vortex beams [23,24].

In this paper, we design a single-photon polarizing Sagnac interferometer with a liquid crystal (LC), which provides a stable and simple way to manipulate only one path of the SI instead of the two paths of the SI. The more types of the vortex beams' interference is researched and analyzed in the SI. By precisely varying the SI phase, the TC of OAM, and the measurement basis, we experimentally observe the interferograms of the initial states in the laser and a single-photon illumination. The resulting interferograms can determine the TC of the input vortex beams. In particular, for the mixed-mode OAM states, our scheme can distinguish the photons carrying positive- and negative-valued TC. These contributions not only provide theoretical support for OAM states

*Corresponding email: Anningzhang@bit.edu.cn

as the quantum information carriers, but also bring the need for device capabilities to detect and efficiently manipulate the OAM states.

II. THEORY

We prepared three single-photon types of OAM states combined with SAM. They are formulated as follows:

$$
\begin{aligned}
|\Phi\rangle &= \frac{1}{2}(|m\rangle + |-m\rangle)|H\rangle - \frac{i}{2}(|m\rangle - |-m\rangle)|V\rangle, \\
|\Psi\rangle &= \frac{1}{\sqrt{2}}(|m\rangle|H\rangle + i|-m\rangle|V\rangle), \\
|\Theta\rangle &= \frac{1}{\sqrt{2}}(|m\rangle|H\rangle + |m\rangle|V\rangle),
\end{aligned} \tag{1}
$$

where, $|H\rangle(|V\rangle)$ denotes the horizontal (vertical) photon polarization and $|\pm m\rangle$ represents the photon states with OAM of $|\pm m\hbar\rangle$. The first state $|\Phi\rangle$ represents the mixed-mode OAM state [25] and contains several components with different values of TC. The second state $|\Psi\rangle$ is the conjugate-mode OAM state [24] and contains two components with equal value, but a diverse sign of TC. The last state $|\Theta\rangle$ represents the single-mode OAM state, which contains two components with equal value and equal sign of TC (details of the preparation can be found in Appendix A). According to the above preparation, we study the measurement technique for three types of OAM states using interference based on the SI.

As a good approximation, Laguerre-Gaussian (LG) modes are most commonly used to describe the optical vortex beams. The amplitude $\mathrm{LG}_{p,m}$ of the optical field can be expressed in a cylindrical coordinate system $r = (\rho, \psi, z)$ given by [26,27]

$$
E_0(r, \phi) = \mathrm{LG}_{p,m} e^{im\phi}, \tag{2}
$$

$$
\begin{aligned}
\mathrm{LG}_{p,m} = &\sqrt{\frac{2p!}{\pi(p+|m|)!}} \frac{1}{\omega(z)} \left[\frac{r\sqrt{2}}{\omega(z)}\right]^{|m|} \exp\left[\frac{-r^2}{\omega(z)^2}\right] L_p^{|m|} \\
&\times \left(\frac{2r^2}{\omega(z)^2}\right) \exp\left[\frac{ik_0 r^2 z}{2\left(z^2 + z_R^2\right)}\right] \\
&\times \exp\left[-i(2p + |m| + 1)\tan^{-1}\left(\frac{z}{z_R}\right)\right],
\end{aligned} \tag{3}
$$

where the $L_p^{|m|}$ is the normalized Laguerre polynomial, with the azimuthal index m and radial index p. The azimuthal index m corresponds to the beam OAM $m\hbar$ per photon and may take any integer value, either positive or negative. The radial index $p \geqslant 0$ specifies the number of rings in the radial intensity distribution. The z relies on the Gaussian envelope, with the parameters of the Rayleigh range z_R and width $\omega(z)$ given by

$$
\omega(z) = \omega_0 \sqrt{1 + \left(\frac{2z}{k_z \omega_0^2}\right)}, \quad z_R = \frac{k_z \omega_0^2}{2}, \tag{4}
$$

where $\omega_0 = \omega(0)$ is the beam radius at focus. Subsequently, the LG beams are directed to a modified SI consisting of three mirrors and a phase controller. The ideal experiment is show in Fig. 1. The polarized beam splitter (PBS) divides the LG beams into two paths. One of the light fields can be expressed as $E_1(r, \phi) = \mathrm{LG}_{p,m_1} e^{im_1\phi}$. While the expression of the opposite light field for the LG beam can be written as $E_2(r, \phi) = \mathrm{LG}_{p,m_2} e^{im_2\phi} e^{i\theta}$, where $e^{i\theta}$ is the phase difference added by a LC, which changes only one path instead of both paths. Thus, our scheme is more practical and easier to modulate the vortex beam than the scheme used in the DP in the SI. After two beams combine again on the PBS, the total light field becomes

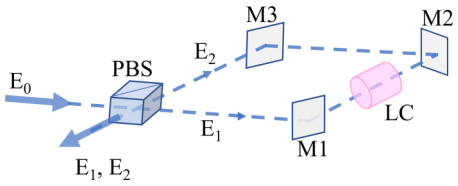

FIG. 1. The schematic diagram of the modified Sagnac interferometer in which relative phase $e^{i\theta}$ is introduced by the liquid crystal (LC)

$$
E_3(r, \phi) = E_1(r, \phi) + E_2(r, \phi). \tag{5}
$$

The more theoretical, analytical derivation details are shown in Appendix B. When the LG beam with single mode is an input state, the intensity distribution of the interferogram is $I = 2\mathrm{LG}_{p,m}^2[1 + \cos(\theta)]$; it is manifested that there would be no changes in the helicity of OAM associated with the input LG mode. For the input state of the LG beam with conjugate mode $m_2 = -m_1$, the intensity distribution $I = 2\mathrm{LG}_{p,m}^2[\cos(2m\phi + \theta)]$ implies a rotation of the intensity pattern of $2m$ pedals with rotation angle $\Delta\phi = \Delta\theta/2m$. For the mixed-mode LG beams, the intensity distribution we obtain $I = 2\mathrm{LG}_{p,m_1}^2[1 + \sin(\theta)] + 2\mathrm{LG}_{\mathrm{p,m_1}}\mathrm{LG}_{\mathrm{p,m_2}}[2\cos(\theta)(\mathrm{m_2} - \mathrm{m_1})\phi] + 2\mathrm{LG}_{\mathrm{p,m_2}}^2[1 + \sin(\theta)]$ indicates that we can control the interference pattern by changing the phase difference between two OAM components. In Fig. 2, we plot the numerical results of the intensity interferogram taking $m = 2$. It is easy to see that when the mixed-mode OAM state $|\Phi\rangle$ is injected into the SI, it results in the intensity interferogram with shapes of petals and rings as the change of phase difference. The phases $\Delta\theta = \pi/2$ and $\Delta\theta = 3\pi/2$ correspond to the rings in the opposite charge of OAM. The other phase is the petal that rotate clockwise. When the conjugate-mode OAM state $|\Psi\rangle$ is injected into the SI, the intensity interferograms are petals.

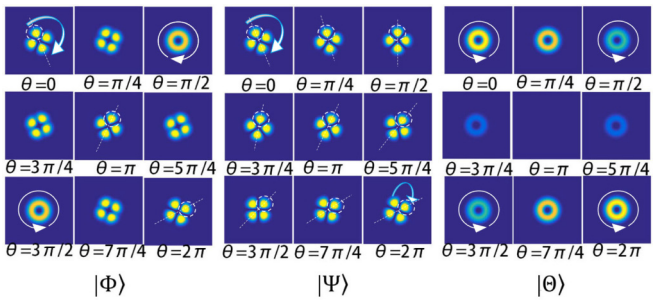

FIG. 2. Numerical results of multimode OAM states' interferograms for mixed mode $|\Phi\rangle$, conjugate mode $|\Psi\rangle$, single mode $|\Theta\rangle$, as the phase difference θ, with $m = 2$ on the basis $H + V$.

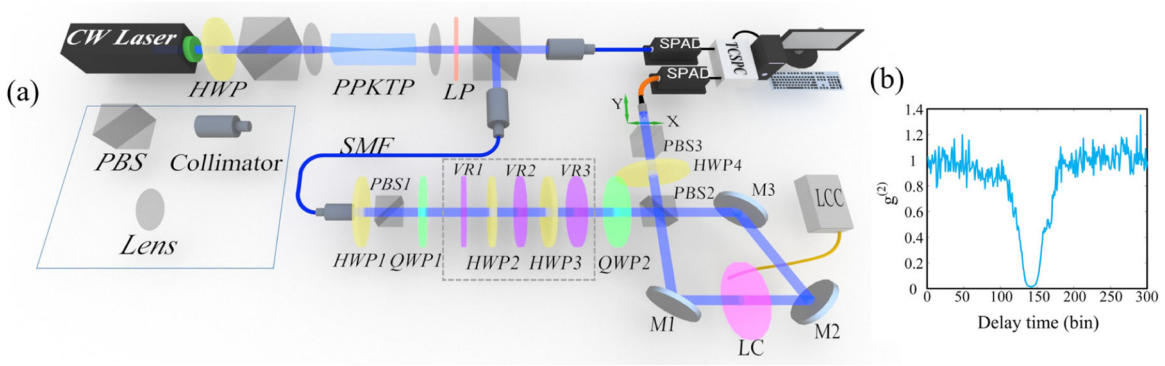

FIG. 3. (a) Experimental setup for single-photon OAM states interferometer. A CW laser with 405 nm pumps a PPKTP crystal to generate SPDC photon pairs with wavelength at 810 nm. One of the pair photons is detected by SPAD as the trigger, another one of the pair photons reflected from PBS is collected by SMF as single-photon source. After HWP1 and PBS1, the single-photon OAM state is generated by VRs, HWPs, and QWPs as shown in the dashed box. The LC induces a phase difference between the $|H\rangle$ and $|V\rangle$ polarized beams in SI, which is controlled by the liquid crystal controller (LCC) by adjusting the voltage of controller to change phase. After the state evolution in SI, the output beam from SI is detected by scanning the fiber system and single-photon detector. PBS3 and HWP4 are used for the measurement basis. (b) The experimental results of the second-order correlation of our single-photon source. There is a clear dip in 142 time bins and every bin is 64 ps.

It rotates with angle $\Delta\phi = \pi/16$ along the positive direction in each period of the phase difference $\Delta\theta = \pi/4$. When the input single-mode OAM state $|\Theta\rangle$ into the SI, the intensity interferograms are rings that brighten the variation.

III. EXPERIMENT

The experimental setup is shown in Fig. 3(a). The overall procedure of our experiment falls into four major parts. In the first part, the heralded single photons at 810 nm are produced via type-II spontaneous parametric down conversion (SPDC), the same as in Refs. [28,29]. A continuous wave (CW) 405-nm diode laser beam with 20 mw of power pumps a periodically poled potassium titanyl phosphate (PPKTP) crystal to generate 810 nm entangled photon pairs. A polarized beam splitter (PBS) separates the entangled photon pairs. One of the photon pairs, which is called the idler photon, is coupled into a single-mode fiber (SMF) by the collimator and connected directly to the single-photon avalanche photodiode (SPAD) as a trigger for the other photon. The other photon, which is called the signal photon, is also coupled into the SMF by the collimator and sent out to the subsequent experimental device as a single-photon source. To validate the performance of the single-photon source, we measure the value of the second-order correlation function $g^{(2)} = 0.0151$ as shown in Fig. 3(b). At the beginning, we carried out laser experiments using an 808-nm fiber laser instead of a single-photon source. In the second part, the initial state encoded with both polarization and the OAM mode was generated by using quarter wave plates (QWP), vortex retarders (VR), and half wave plates (HWP) as shown in the dashed area in Fig. 3(a). The HWP1 and PBS1 were used to control the light intensity. In the state evolution part, the beam enters the SI consisting of three mirrors and PBS2. A single PBS2 serves as the import and export gates of the interferometer. Horizontal ($|H\rangle$) and vertical ($|V\rangle$) components split from the PBS2 and propagate inside the interferometer along the same optical line, but in the opposite directions. A LC is placed in the SI to control the phase differences of $e^{i\theta}$ between the clockwise beam and anticlockwise beam. The two beams merge again and exit from another port of the PBS2. In the measurement part, the HWP4 and PBS3 are used to realize the projection measurement of $H + V/H - V$ (details of the evolution process can be found in Appendix C). In the laser experiment, the interferograms are obtained by a charge coupled device (CCD) with the exposure time of 100 μs.

In the single-photon OAM state experiment, we use the fiber scanning system instead of the CCD. The fiber scanning system consists of four parts: the multimode fiber, single-photon avalanche photodiode (SPAD: SPCM-800-14-FC with 100 cps dark count rate), time-correlated single-photon counting (TCSPC), and two-dimensional motorized linear stage. The OAM photon is collected and detected by the scanning multimode fiber with 100 μm each step. Meanwhile, the TCSPC (siminics FT1040) is used to count all signals from the single-photon detector with 64-ps accuracy.

IV. RESULTS

The laser OAM interference experimental results are shown in Fig. 4. The phase θ raised from 0 to 2π with $\pi/4$ each subgraph by the voltage of LCC.

In the first column, we show the interferogram of the OAM states with $m = 2$ on the basis $H + V$. For the mixed-mode OAM state $|\Phi\rangle$, the effects of phase on interference patterns exhibit two different distributions with rings and clockwise-rotating four petals as the θ increased. The rings' interferogram occurs when the relative phase difference given is $\pi/2$, $3\pi/2$, and it corresponds to the TC values of $m = 2$ and $m = -2$, respectively. Thus, our scheme enables to sort the plus and minus signs of TC in mixed-mode OAM states by controlling the LC phase for the conjugate-mode OAM state $|\Psi\rangle$, which appears only with the four-petal interferogram. In addition, the interference patterns rotate $\Delta\phi = \pi/2$ along the positive direction in the entire period of phase differences $\Delta\theta = 2\pi$. For the single-mode OAM states $|\Theta\rangle$, it appears

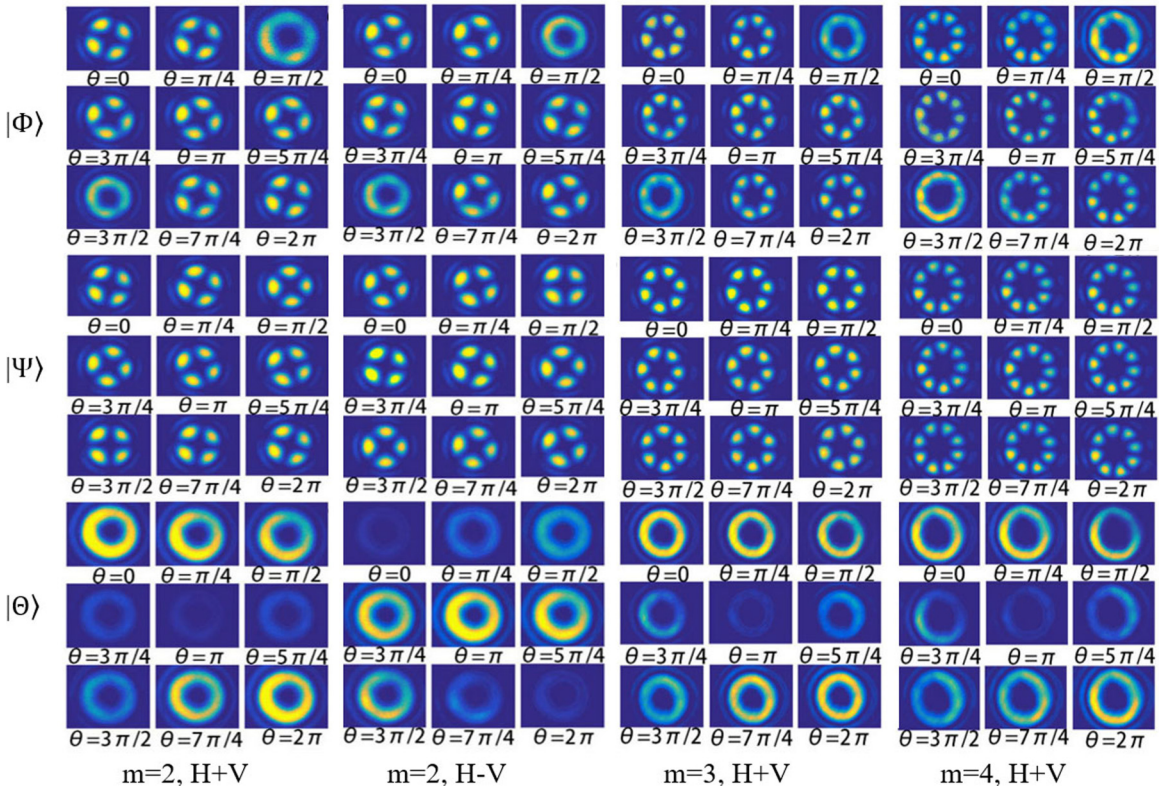

FIG. 4. Experimental results of laser interferograms of multimode OAM states, with the phase difference θ in SI. Each row corresponds to the different initial states $|\Phi\rangle$, $|\Psi\rangle$, $|\Theta\rangle$. The columns correspond to the different OAM initial states states with charge $m = 2, 3, 4$ for the measurement basis $H + V$ and $H - V$.

only with the rings' interferogram. The brightness varies periodically with relative phase θ. First it goes from light to dark, then from dark to light gradually. Obviously, the experimental results are consistent with the result of the numerical simulation analysis shown in Fig. 2. The phase θ determines the shape and rotation of the interference patterns.

In the second column, we show the interferogram of the OAM states with $m = 2$ on the basis $H - V$. For the mixed-mode OAM state $|\Phi\rangle$, with the change-of-phase difference θ, the ring and clockwise rotating four-petal interferograms still appear. The phase $\Delta\theta = \pi/2$, $\Delta\theta = 3\pi/2$ correspond to the rings with a TC value of $m = -2$ and $m = 2$. For the conjugate-mode OAM state $|\Psi\rangle$, the interferogram with four petals rotates along the clockwise direction with rotation angle $\Delta\phi = \pi/16$ for each subgraph. For the single-mode OAM states $|\Theta\rangle$, the interferogram with rings varies from dark to light, then from light to dark gradually. The TC number can be deduced from the petal number by dividing it by 2. By comparing the basis $H + V$ and $H - V$ as shown in the first and second columns it is found that with the phase changes, the interferogram shapes of the three initial states in the basis $H - V$ and $H + V$ is the same. However, the distribution of the intensity corresponding to the phase differences is orthogonal to each other. This is owing to the interferograms corresponding to the projective basis vector are orthogonal.

In the third column, we show the interferogram of the OAM states with $m = 3$ on the basis $H + V$. For the mixed-mode OAM state $|\Phi\rangle$, the interference patterns appear as rings and six petals rotating clockwise. By modulating the phase to $\Delta\theta = \pi/2$ and $\Delta\theta = 3\pi/2$, the positive and negative signs with $m = 3$ and $m = -3$ of TC can be sorted in the mixed mode. For the conjugate-mode OAM state $|\Psi\rangle$, the interferogram with six petals rotates along the clockwise direction. The quantity of petals is double the original value of TC. In addition, the larger the order m, the smaller the rotation angle as the phase θ changes. When $\Delta\theta = \pi/4$, the angle of rotation is $\Delta\phi = \pi/24$. For the single-mode OAM states $|\Theta\rangle$, the size of the ring gets bigger, and becomes larger than the rings with $m = 2$.

In the fourth column, we show the interferogram of the OAM states with $m = 4$ on the basis $H + V$. It can be seen from the mixed-mode OAM state $|\Phi\rangle$ that the rings and clockwise-rotating eight-petal interferograms occur with the change of phase. For the conjugate-mode OAM state $|\Psi\rangle$, the eight petals' interferogram rotates along the clockwise direction. The quantity of petals is twice the original value of TC. When $\Delta\theta = \pi/4$, the angle of rotation becomes $\Delta\phi = \pi/32$. For the single-mode OAM states $|\Theta\rangle$, the brightness of the rings' interferogram varies periodically with relative phase θ. In addition, the size of the rings gets bigger. By comparing the first, third, and fourth columns we find that the TC and rotation of the vortex beam can be deduced from the petals' quantity and size of the rings. All in all, the vortex beams with mixed-, conjugate-, and single-mode OAM states correspond to an individual interference pattern in the change of the relative phases. In addition, the three initial states can be classified

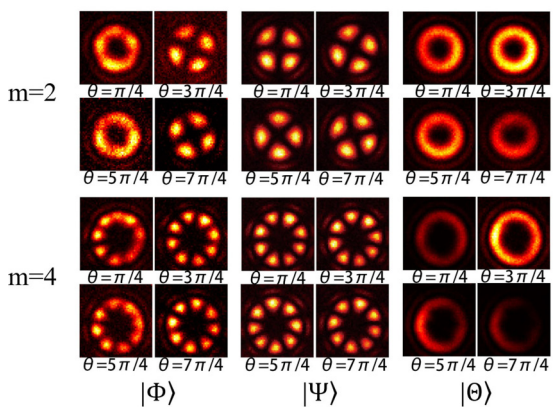

FIG. 5. Single-photon interferograms obtained by scanning coupling fiber. Each column corresponds to the initial state $|\Phi\rangle$, $|\Psi\rangle$, $|\Theta\rangle$, as the phase difference θ on the basis $H+V$. The top and next two rows correspond to TC with $m=2$ and $m=4$.

with good precision for different phases. The more theoretical simulations of the experiment for the cases presented in Fig. 4 are shown in Appendix C.

To demonstrate that our device works at the single-photon level, we carry out the experiment with the use of a single-photon sources. The interferograms are reconstructed from two coincidence counts obtained by scanning coupling fibers. The fiber-optical scanning system was mounted in a displacement platform with bi-dimensionality. It can scan a line regularly, first moved 100 μm each step from left to right, and then shifted 100 μm to the next line for continued scanning. At first, the ideal scan range was found by exploiting laser beams by scanning a relatively large-ranged area. We specify a scan area of $5\times 5\,\mathrm{mm}^2$, which is equal to 2500 pixels. In our experiment, approximately 18 000 photons are detected for each figure in the time of 14 400 s.

The single-photon OAM interference experimental results are shown in Fig. 5. We measured the interferograms of the single photon for generated OAM states with $m=2,4$, by choosing four typical relative phases with $\pi/4$, $3\pi/4$, $5\pi/4$, and $7\pi/4$, under the basis of $H+V$. For the mixed-mode OAM state $|\Phi\rangle$, as is shown in the first column in Fig. 5, its interferogram appears with two distributions with the change-of-phase difference θ. When the phase is $\Delta\theta=\pi/4$, $\Delta\theta=5\pi/4$, the interferograms are rings with the opposite value of TC. When the phase is $\Delta\theta=3\pi/4$, $\Delta\theta=5\pi/4$, the interferograms are petals. For the conjugate-mode OAM state $|\Psi\rangle$, as shown the second column in Fig. 5, we obtained four and eight petals that rotate clockwise to the phase difference θ. For the single-mode OAM state $|\Theta\rangle$, as shown in the third column of Fig. 5, the rings' interferograms observed changes regularly from pale to bright and then from bright to dark. In addition, the petals' number and the size of the rings also increases as m increases. Moreover, we notice that there is a fixed phase difference of almost $5\pi/4$ between the single-photon interferogram and the laser interferogram. This is attributed to the fact that the laser wavelength is 808 nm, while the single photon is 810 nm. The slight difference in wavelength leads to stable differences in the interferometer paths, which leads to phase differences. In total, the experimental results indicate

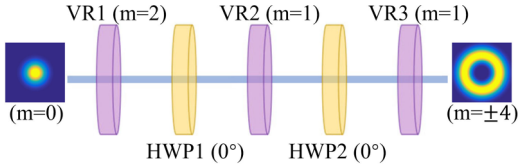

FIG. 6. The schematic of preparing OAM modes with charge $m=\pm 4$.

that the detection of the single-photon OAM state is efficient based on the SI. This allows us access to a larger state space for quantum computing and communication applications.

V. SUMMARY

In summary, we constructed a polarizing SI to investigate the interference effects of three types of OAM states for mixed-mode $|\Phi\rangle$, conjugate-mode $|\Psi\rangle$, and single-mode $|\Theta\rangle$ in the single-photon and laser regimes. By adjusting the SI to different phases, we observed a different interference pattern for individual OAM states both experimentally and numerically. The results showed that the scheme was capable of estimating the TC of the vortex beam. In addition, our scheme also offers a possible method to sort photons with opposite signs of TC in the mixed-mode OAM state by fixing the phase of the SI. The research of single-photon interference effects of OAM states based on the SI opens up an alternative idea for detecting single-photon vortex beams. In addition, these results enrich our understanding of multiple vortex beams' interference.

ACKNOWLEDGMENT

This work is supported by National Key R & D Program of China (Grant No. 2018YFB0504303).

APPENDIX A: STATE GENERATION METHODS FOR SINGLE-PHOTON OAM STATES

In our experiment, we use a vortex retarder (VR) [30] to generate different modes of the single-photon vortex beam. VR acts as a "coupler" of the two types of optical angular momentum, SAM (i.e., polarization) and OAM. In general, the function for an m-order VR allows their conversion into each other according to the following rules [31]:

$$\begin{aligned} |m'\rangle|R\rangle &\xrightarrow{m-\text{order VR}} |m'+m\rangle|L\rangle, \\ |m'\rangle|L\rangle &\xrightarrow{m-\text{order VR}} |m'-m\rangle|R\rangle. \end{aligned} \tag{A1}$$

Here, the $|\pm m\rangle$ represents the TC of the spatial field. The sign of m depends on the handedness of the input polarization, with $|L\rangle=(|H\rangle-i|V\rangle)/\sqrt{2}$ and $|R\rangle=(|H\rangle+i|V\rangle)/\sqrt{2}$ being the left and right circularly polarized states, respectively. We obtained higher OAM modes by virtue of a cascade transformation, in which an input SAM modes possessed of $m=0$ can sequentially transverse into an OAM beam with $m=\pm 2,\pm 3,\pm 4$ by the aid of VRs and HWP. Take the transformation SAM $\rightarrow$ OAM ($m=\pm 4$) as an example as shown

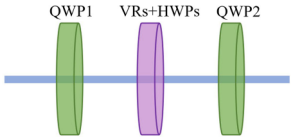

FIG. 7. The schematic of preparing single-photon multimode OAM states.

in Fig. 6, which can be formulated in the following way:

$$\begin{aligned}
&|0\rangle|R\rangle \overset{\mathrm{VR}_1(m=2)}{\longrightarrow} |2\rangle|L\rangle \overset{\mathrm{HWP}=0^\circ}{\longrightarrow} |2\rangle|R\rangle \overset{\mathrm{VR}_2(m=1)}{\longrightarrow} |3\rangle|L\rangle \\
&\quad \overset{\mathrm{HWP}=0^\circ}{\longrightarrow} |3\rangle|R\rangle \overset{\mathrm{VR}_3(m=1)}{\longrightarrow} |4\rangle|L\rangle, \\
&|0\rangle|L\rangle \overset{\mathrm{VR}_1(m=2)}{\longrightarrow} |-2\rangle|R\rangle \overset{\mathrm{HWP}=0^\circ}{\longrightarrow} |-2\rangle|L\rangle \overset{\mathrm{VR}_2(m=1)}{\longrightarrow} \\
&\quad \times |-3\rangle|R\rangle \overset{\mathrm{HWP}=0^\circ}{\longrightarrow} |-3\rangle|L\rangle \overset{\mathrm{VR}_3(m=1)}{\longrightarrow} |-4\rangle|R\rangle.
\end{aligned} \tag{A2}$$

Meanwhile, the three SAM-OAM states prepared by changing the angle of QWPs is shown in Fig. 7 for convenience to encode the information. The first SAM-OAM correlated state can be formulated as follows:

$$\begin{aligned}
|\Phi\rangle \propto |H\rangle &\overset{\mathrm{QWP1}=0^\circ}{\longrightarrow} |H\rangle = \frac{1}{\sqrt{2}}(|R\rangle + |L\rangle) \overset{\mathrm{VRs+HWPs}}{\longrightarrow} \\
&\times \frac{1}{\sqrt{2}}(|m\rangle|L\rangle + |-m\rangle|R\rangle) = \frac{1}{2}(|m\rangle + |-m\rangle)|H\rangle \\
&- \frac{i}{2}(|m\rangle - |-m\rangle)|V\rangle.
\end{aligned} \tag{A3}$$

The mixed-mode OAM state $|\Phi\rangle$ generated is first prepared linearly by polarized photons passing through the VRs + HWPs combination for different OAM modes. The QWP(0°) is placed in front for convenience for the other states' preparation. The conjugate-mode OAM state $|\Psi\rangle$ is achieved by varying the above initial state polarization from a circular to a linear basis with a QWP oriented at -45° with respect to the horizontal axis, then it can be expressed as

$$\begin{aligned}
|\Psi\rangle \propto |H\rangle &\overset{\mathrm{QWP1}=0^\circ}{\longrightarrow} |H\rangle = \frac{1}{\sqrt{2}}(|R\rangle + |L\rangle) \overset{\mathrm{VRs+HWPs}}{\longrightarrow} \\
&\times \frac{1}{\sqrt{2}}(|m\rangle|L\rangle + |-m\rangle|R\rangle) \overset{\mathrm{QWP2}=-45^\circ}{\longrightarrow} \frac{1}{\sqrt{2}}(|m\rangle|H\rangle \\
&+ i|-m\rangle|V\rangle).
\end{aligned} \tag{A4}$$

The i is a relative phase after the transformation of the QWP. The single-mode OAM state $|\Theta\rangle$ is prepared via the photon being horizontally polarized and passing through the first quarter wave plate QWP oriented at -45° transforming the spin to right-circular polarization, then the VR implements the spin to OAM conversion, the final QWP at 0° transforms it back to $|H\rangle$ and $|V\rangle$, respectively,

$$\begin{aligned}
|\Theta\rangle \propto |H\rangle &\overset{\mathrm{QWP1}=-45^\circ}{\longrightarrow} |R\rangle \overset{\mathrm{VRs+HWPs}}{\longrightarrow} |m\rangle|L\rangle \\
&\overset{\mathrm{QWP2}=0^\circ}{\longrightarrow} \frac{1}{\sqrt{2}}(|m\rangle|H\rangle + |m\rangle|V\rangle).
\end{aligned} \tag{A5}$$

Compared with the quantum states in a single Degree of freedom (DOF), the combination of two DOFs as an ideal carrier has made an important development in the study of quantum systems and their applications.

APPENDIX B: THEORETICAL EVOLUTION OF SINGLE-PHOTON OAM STATES IN THE SAGNAC INTERFEROMETER

Consider the OAM light carrying m_1, m_2 passing through a SI. The output light field can be express as

$$\begin{aligned}
E_3(r,\phi) = E_1(r,\phi) + E_2(r,\phi) &= LG_{p,m_1} e^{im_1\phi} \\
&+ \mathrm{LG}_{p,m_2} e^{im_2\phi} e^{i\theta},
\end{aligned} \tag{B1}$$

where $e^{i\theta}$ is the phase difference between the two arms of the SI. The intensity of the output beam is

$$\begin{aligned}
I = |E_3(r,\phi)|^2 &= [\mathrm{LG}_{p,m_1} e^{im_1\phi} + \mathrm{LG}_{p,m_2} e^{im_2\phi + i\theta}] \\
&\times [\mathrm{LG}_{p,m_1} e^{-im_1\phi} + \mathrm{LG}_{p,m_2} e^{-im_2\phi - i\theta}] \\
&= {\mathrm{LG}_{p,m_1}}^2 + \mathrm{LG}_{p,m_1}\mathrm{LG}_{p,m_2}[e^{-i(m_2-m_1)\phi} e^{-i\theta} \\
&+ e^{i(m_2-m_1)\phi} e^{i\theta}] + {\mathrm{LG}_{p,m_2}}^2 \\
&= {\mathrm{LG}_{p,m_1}}^2 + {\mathrm{LG}_{p,m_2}}^2 + \mathrm{LG}_{p,m_1}\mathrm{LG}_{p,m_1} \\
&\times \{2\cos[(m_2 - m_1)\phi + \theta]\},
\end{aligned} \tag{B2}$$

when taking $\mathrm{LG}_{p,m_1} = \mathrm{LG}_{p,m_2}$ and the single-mode LG beams with OAM of $m_2 = m_1$ inject into SI, then the intensity of Eq. (B2) becomes

$$I = 2\mathrm{LG}_{p,m}^2[1 + \cos(\theta)]. \tag{B3}$$

It can be seen that the intensity distribution is independent of the helicity of OAM (m) associated with the input LG beam, but with phase difference (θ) between the two arms of the SI. Thus, the ring interferogram appears. When the conjugate-mode LG beams with the OAM of $m_2 = -m_1$ injected into the SI, the intensity of Eq. (B2) becomes

$$I = 2\mathrm{LG}_{p,m}^2[\cos(2\mathrm{m}\phi + \theta)]. \tag{B4}$$

It is indicated that there is a rotation of the intensity pattern of $2m$ petals with rotation angle $\Delta\phi = \Delta\theta/2m$. Consider the case where the LG beams with mixed-mode OAM of $m_1 + m_2$, $m_1 - m_2$ passes through a SI. The electric field of E_1, E_2 can be expressed as

$$\begin{aligned}
E_1(r,\phi) &= \mathrm{LG}_{p,m_1} e^{im_1\phi} + \mathrm{LG}_{p,m_2} e^{im_2\phi}, \\
E_2(r,\phi) &= (-\mathrm{iLG}_{p,m_1} e^{im_1\phi} + \mathrm{iLG}_{p,m_2} e^{im_2\phi}) e^{i\theta}.
\end{aligned} \tag{B5}$$

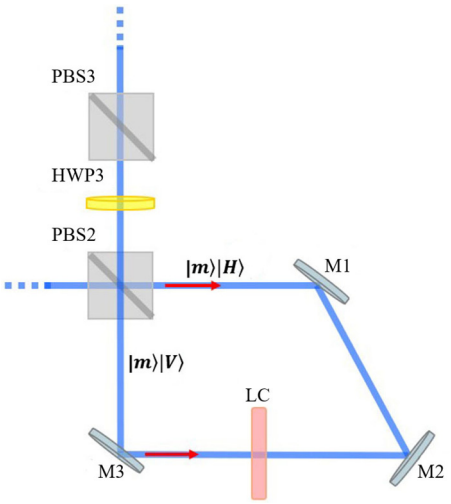

FIG. 8. Schematic diagram of single-photon multiple OAM states' evolution process.

Then we can obtain the intensity as

$$\begin{aligned} I &= |E_1(r,\phi)+E_2(r,\phi)|^2 = [(1-ie^{i\theta})\mathrm{LG}_{p,m_1}e^{im_1\phi} \\ &\quad + (1+ie^{i\theta})\mathrm{LG}_{p,m_2}e^{im_2\phi}][(1+ie^{-i\theta})\mathrm{LG}_{p,m_1}e^{-im_1\phi} \\ &\quad + (1-ie^{-i\theta})\mathrm{LG}_{p,m_2}e^{-im_2\phi}] \\ &= 2\mathrm{LG}^2_{p,m_1}[1+\sin(\theta)] + \mathrm{LG}_{p,m_1}\mathrm{LG}_{p,m_2}[-i(e^{-i\theta}+e^{i\theta}) \\ &\quad \times e^{-i(m_2-m_1)\phi} + i(e^{i\theta}-e^{-i\theta})e^{i(m_2-m_1)\phi}] + 2\mathrm{LG}^2_{p,m_2} \\ &\quad \times [1+\sin(\theta)] \\ &= 2\mathrm{LG}^2_{p,m_1}[1+\sin(\theta)] + 2\mathrm{LG}_{p,m_1}\mathrm{LG}_{p,m_2}[2\cos(\theta)(\mathrm{m}_2 \\ &\quad - m_1)\phi] + 2\mathrm{LG}^2_{p,m_2}[1+\sin(\theta)], \end{aligned} \tag{B6}$$

It can be seen when taking $\theta = \pi/2$ and $\theta = 2\pi/3$ that the intensity distribution is independent of m. Thus, the interferogram remains a ring. In the other cases of θ, there would be a change in the helicity of the intensity pattern. The theoretical expression clearly reveals the relationship between the mode component m and phase θ of the LG beams.

APPENDIX C: EXPERIMENTAL EVOLUTION OF SINGLE-PHOTON OAM STATES IN THE SAGNAC INTERFEROMETER

As is shown in Fig. 8, we measure OAM states by designing a quite stable and adjustable SI. Taking the input state $|\Theta\rangle = \frac{1}{\sqrt{2}}(|m\rangle|H\rangle + |m\rangle|V\rangle)$ as an example, the specific evolution is as follows:

$$\begin{aligned} |\Theta\rangle &= \frac{1}{\sqrt{2}}(|m\rangle|H\rangle + |m\rangle|V\rangle) \xrightarrow{\mathrm{PBS2}(T)} \frac{1}{\sqrt{2}}|m\rangle|H\rangle \xrightarrow{M_3} \\ &\quad \times \frac{1}{\sqrt{2}}|-m\rangle|H\rangle \xrightarrow{M_2} \frac{1}{\sqrt{2}}|m\rangle|H\rangle \xrightarrow{\mathrm{LC}} \frac{1}{\sqrt{2}}|m\rangle|H\rangle e^{i\theta} \\ &\xrightarrow{M_1} \frac{1}{\sqrt{2}}|-m\rangle|H\rangle e^{i\theta} \xrightarrow{\mathrm{PBS2}} \frac{1}{\sqrt{2}}|-m\rangle|H\rangle e^{i\theta}. \end{aligned} \tag{C1}$$

Because the total number of polarized beams reflected from PBS2 and the mirror is odd, the OAM sign changes

$$\begin{aligned} |\Theta\rangle &= \frac{1}{\sqrt{2}}(|m\rangle|H\rangle + |m\rangle|V\rangle) \xrightarrow{\mathrm{PBS2}(R)} \frac{i}{\sqrt{2}}|-m\rangle|V\rangle \\ &\xrightarrow{M_1} \frac{i}{\sqrt{2}}|m\rangle|V\rangle \xrightarrow{\mathrm{LC}} \frac{i}{\sqrt{2}}|m\rangle|V\rangle \xrightarrow{M_2} \frac{i}{\sqrt{2}}|-m\rangle|V\rangle \\ &\xrightarrow{M_3} \frac{i}{\sqrt{2}}|m\rangle|V\rangle \xrightarrow{\mathrm{PBS2}} \frac{1}{\sqrt{2}}|-m\rangle|V\rangle. \end{aligned} \tag{C2}$$

Note that in the above equation T (R) represents transmission (reflection) and HWP3 and PBS3 are used to realize the projection measurement of $H+V/H-V$. Then the above states become

$$\begin{aligned} &\frac{1}{\sqrt{2}}|-m\rangle|H\rangle e^{i\theta} + \frac{1}{\sqrt{2}}|-m\rangle|V\rangle \xrightarrow{\mathrm{HWP3=22.5^\circ}} \frac{1}{\sqrt{2}}|-m\rangle \\ &\quad \times (|H\rangle + |V\rangle)e^{i\theta} + \frac{1}{\sqrt{2}}|-m\rangle(|H\rangle - |V\rangle) \xrightarrow{\mathrm{PBS3}} \\ &\quad \times \frac{1}{\sqrt{2}}(|-m\rangle + |-m\rangle e^{i\theta})|H\rangle \\ &\quad \times \frac{1}{\sqrt{2}}|-m\rangle|H\rangle e^{i\theta} + \frac{1}{\sqrt{2}}|-m\rangle|V\rangle \xrightarrow{\mathrm{HWP2=-22.5^\circ}} \frac{1}{\sqrt{2}}|-m\rangle \\ &\quad \times (-|H\rangle + |V\rangle)e^{i\theta} + \frac{1}{\sqrt{2}}|-m\rangle(|H\rangle + |V\rangle) \xrightarrow{\mathrm{PBS3}} \\ &\quad \times \frac{1}{\sqrt{2}}(|-m\rangle - |-m\rangle e^{i\theta})|H\rangle, \end{aligned} \tag{C3}$$

where $\frac{1}{\sqrt{2}}(|-m\rangle + |-m\rangle e^{i\theta})|H\rangle$ and $\frac{1}{\sqrt{2}}(|-m\rangle - |-m\rangle e^{i\theta})|H\rangle$ is the final state that can be observed, which also can be seen as a measurement in the $|L\rangle$, $|R\rangle$ polarization basis. Similarly, the other final states are

$$\begin{aligned} |\Phi\rangle &\xrightarrow{\mathrm{HWP3}(22.5^\circ)+\mathrm{PBS3}} \frac{1}{2}[(i+e^{i\theta})|m\rangle - (i-e^{i\theta})|-m\rangle]|H\rangle, \\ |\Phi\rangle &\xrightarrow{\mathrm{HWP3}(-22.5^\circ)+\mathrm{PBS3}} \frac{1}{2}[(i-e^{i\theta})|m\rangle - (i+e^{i\theta})|-m\rangle]|H\rangle, \\ |\Psi\rangle &\xrightarrow{\mathrm{HWP3}(22.5^\circ)+\mathrm{PBS3}} \frac{1}{\sqrt{2}}(i|m\rangle + |-m\rangle e^{i\theta})|H\rangle, \\ |\Psi\rangle &\xrightarrow{\mathrm{HWP3}(-22.5^\circ)+\mathrm{PBS3}} \frac{1}{\sqrt{2}}(i|m\rangle - |-m\rangle e^{i\theta})|H\rangle. \end{aligned} \tag{C4}$$

Notably, we do not convert states $|\Phi\rangle$, $|\Psi\rangle$, and $|\Theta\rangle$ to the fundamental Gaussian mode for a projection measurement as was used in previous works [32,33]. Photons of the three states are emitted from the same end of PBS3 and directly received by the optical fiber scanning system for imaging to measure the photon distribution in the entire space, which can be more comprehensive and intuitive to obtain all information without information loss for all OAM modes. This can be most effective for detecting the OAM modes of the vortex beam more accurately than previous methods.

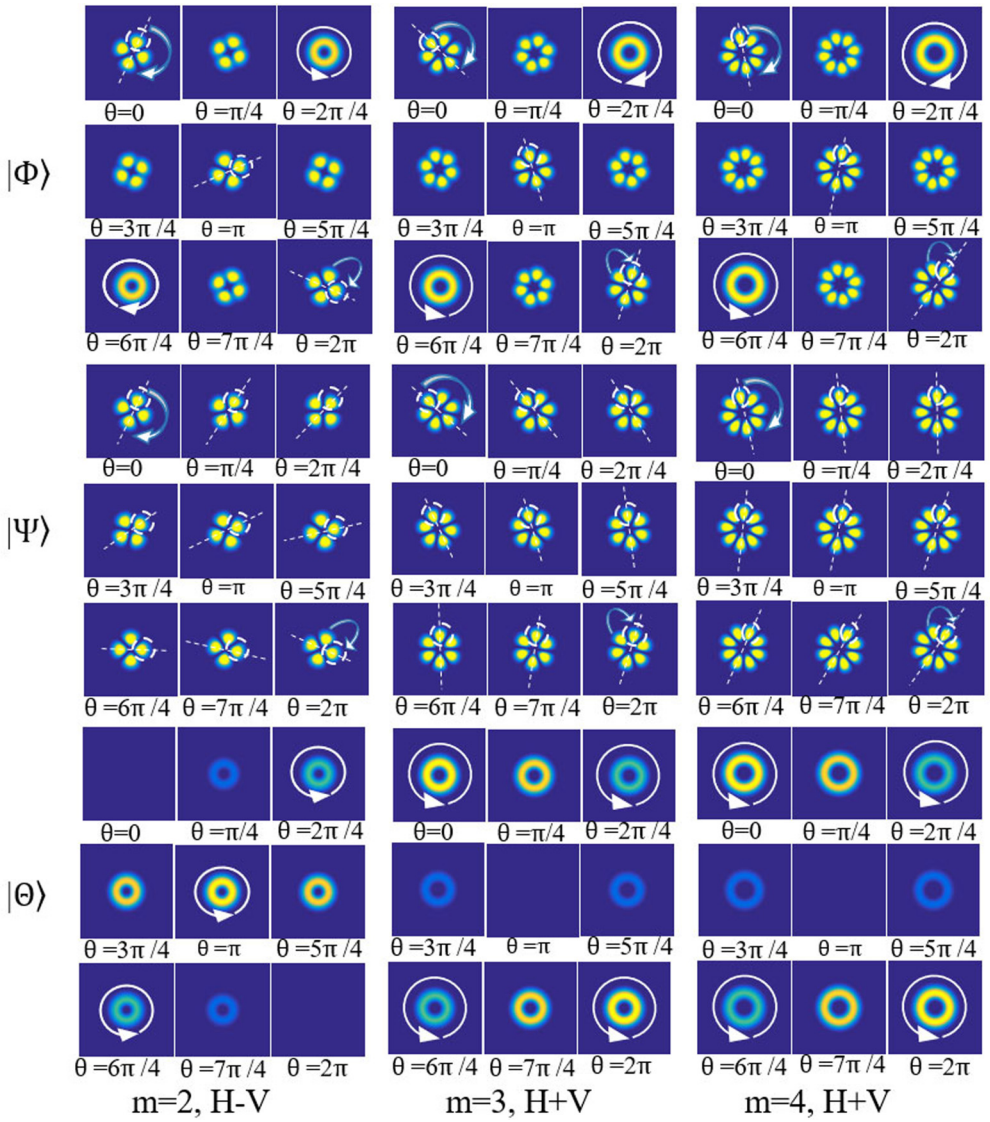

FIG. 9. Numerical results of multimode OAM states' interferograms for mixed mode $|\Phi\rangle$, conjugate mode $|\Psi\rangle$, single mode $|\Theta\rangle$, as the phase difference θ, with $m = 2, 3, 4$ for the measurement basis $H + V$ and $H - V$.

In Fig. 9, we present more theoretical simulation results for the case shown in Fig. 4. In the first column, we plot the intensity interferogram of three OAM states, as the phase difference θ on the basis $H - V$. The clockwise curve indicates the direction of the petal rotation, and the circle with the clockwise and anticlockwise directions indicates the positive and negative modes of OAM. Obviously, the simulation results are consistent with the experimental result for the three OAM states as is shown in the second column of Fig. 4. The interferogram is orthogonal for the measurement bases $H + V$ and $H - V$ with $m = 2$. In the second and third columns, we plot the intensity interferogram of the three OAM states, as the phase difference θ with $m = 3$ and $m = 4$ on the basis $H + V$. With the increase of TC, the more petals appear in the interferogram and the size of the ring becomes bigger. Based on the above relationship, we can qualitatively judge the TC from the interference intensity. The simulation results are consistent with the experimental results as shown in the third and fourth columns of Fig. 4. The slight difference in the petals' distribution between the experiment and the theory is mainly caused by the alignment and positioning of the wave plates and the vortex plates in the experiment. This result offers a practical and simple way for stable manipulating and measuring the high-dimensional photonic states and provides some theoretical and experimental support for OAM as a quantum information carrier.

[1] L. Allen, M. W. Beijersbergen, R. Spreeuw *et al.*, Orbital angular momentum of light and transformation of Laguerre Gaussian Laser modes, Phys. Rev. A **45**, 8185 (1992).

[2] L. Allen, V. E. Lembessis, and M. Babiker, Spin-orbit coupling in free-space Laguerre-Gaussian light beams, Phys. Rev. A **53**, R2937 (1996).

[3] G. Molina-Terriza, J. P. Torres, and L. Torner, Twisted photons, Nat. Phys. **3**, 305 (2007).

[4] Y. Yan, G. Xie, M. Lavery *et al.*, High-capacity millimetre-wave communications with orbital angular momentum multiplexing, Nat. Commun. **5**, 4876 (2014).

[5] Y. Ren, L. Li, Z. Wang *et al.*, Orbital angular momentum-based space division multiplexing for high-capacity underwater optical communications, Sci. Rep. **6**, 33306 (2016).

[6] M. F. Andersen, C. Ryu, P. Clade *et al.*, Quantized Rotation of Atoms From Photons with Orbital Angular Momentum, Phys. Rev. Lett. **97**, 170406 (2006).

[7] H. Bechmann-Pasquinucci and A. Peres, Quantum Cryptography with 3-State Systems, Phys. Rev. Lett. **85**, 3313 (2000).

[8] L. Zhang, C. Silberhorn, and I. A. Walmsley, On Secure Quantum Key Distribution using Continuous Variables of Single Photons, Phys. Rev. Lett. **100**, 110504 (2008).

[9] J. Leach, M. J. Padgett, S. M. Barnett *et al.*, Measuring the Orbital Angular Momentum of a Single Photon, Phys. Rev. Lett. **88**, 257901 (2002).

[10] P. Li, B. Wang, X. Song *et al.*, Non-destructive identification of twisted light, Opt. Lett. **41**, 1574 (2016).

[11] X. Guo, Z. Meng, J. Li, J. Z. Yang, M. Aili, and A. N. Zhang, The interference properties of single photon vortex beams in Mach-Zehnder interferometer, Appl. Phys. Lett. **119**, 011103 (2021).

[12] S. W. Cui, B. Xu *et al.*, Determining topological charge based on an improved Fizeau interferometer, Opt. Express **27**, 12774 (2019).

[13] H. I. Sztul and R. R. Alfano, Double-slit interference with Laguerre-Gaussian beams, Opt. Lett. **31**, 999 (2006).

[14] Q. Zhao, M. Dong, Y. H. Bai, and Y. Yang, Measuring high orbital angular momentum of vortex beams with an improved multipoint interferometer, Photonics Res. **8**, 745 (2020).

[15] P. Kumar and N. K. Nishchal, Self-referenced interference of laterally displaced vortex beams for topological charge determination, Opt. Commun. **459**, 125000 (2020).

[16] B. Lan, C. Liu, D. Rui, M. Chen, F. Shen, and H. Xian, The topological charge measurement of vortex beam based on dislocation self-reference interferometry, Phys. Scr. **94**, 055502 (2019).

[17] S. Slussarenko, V. DAmbrosio, B. Piccirillo *et al.*, The Polarizing Sagnac Interferometer: A tool for light orbital angular momentum sorting and spin-orbit photon processing, Opt. Express **18**, 27205 (2010).

[18] F.-X. Wang, C. Wei, P. L. Ya *et al.*, Single-path Sagnac interferometer with Dove prism for orbital-angular-momentum photon manipulation, Opt. Express **25**, 24946 (2017).

[19] M. V. Jabir, N. A. Chaitanya, M. Mathew *et al.*, Direct transfer of classical non-separable state into hybrid entangled two photon state, Sci. Rep. **7**, 7331 (2017).

[20] S. Xiao, L. Zhang, D. Wei, F. Liu, Y. Zhang, and M. Xiao, Orbital angular momentum-enhanced measurement of rotation vibration using a Sagnac interferometer, Opt. Express **26**, 1997 (2018).

[21] J.-D. Zhang, Z.-J. Zhang, L.-Z. Cen, J.-Y. Hu, and Y. Zhao, Super-resolved angular displacement estimation based upon a Sagnac interferometer and parity measurement, Opt. Express **28**, 4320 (2020).

[22] F.-X. Wang, W. Juan, C. Wei *et al.*, Controlled-phase manipulation module for orbital-angular-momentum photon states, Opt. Lett. **43**, 349 (2018).

[23] P. Kumar and N. K. Nishchal, Modified Mach–Zehnder interferometer for determining the high-order topological charge of Laguerre–Gaussian vortex beams, J. Opt. Soc. Am. A **36**, 1447 (2019).

[24] Q. Jia, X. Qiu, Z. Wu, W. Zhang, and L. Chen, Transferring linear motion of an optical wedge to rotational frequency shift in an orbital angular momentum interferometer, Appl. Phys. Lett. **111**, 091102 (2017).

[25] E. Karimi, J. Leach, S. Slussarenko, S. Slussarenko, B. Piccirillo, L. Marrucci, L. Chen, W. She, S. Franke-Arnold, M. J. Padgett, and E. Santamato, Spin-orbit hybrid entanglement of photons and quantum contextuality, Phys. Rev. A **82**, 022115 (2010).

[26] L. Allen, M. J. Padgett, and M. Babiker, IV The Orbital Angular Momentum of Light, Prog. Opt. **39**, 291 (1999).

[27] M. Lax and W. H. Louisell, From Maxwell to parazial optics, Phys. Rev. A **11**, 1365 (1975).

[28] J. Z. Yang, M. F. Li, X. X. Chen, W. K. Yu, and A. N. Zhang, Single-photon quantum imaging via single-photon illumination, Appl. Phys. Lett. **117**, 214001 (2020).

[29] X. X. Chen, J. Z. Yang, X. D. Chai, and A. N. Zhang, Single-photon Bell state measurement based on a quantum random walk, Phys. Rev. A **100**, 042302 (2019).

[30] A. Rubano, F. Cardano, B. Piccirillo *et al.*, Q-plate technology: a progress review, J. Opt. Soc. Am. B **36**, D70 (2019).

[31] L. Marrucci, C. Manzo, and D. Paparo, Optical Spin-to-Orbital Angular Momentum Conversion in Inhomogeneous Anisotropic Media, Phys. Rev. Lett. **96**, 163905 (2006).

[32] E. Nagali, L. Sansoni, F. Sciarrino, F. D. Martini *et al.*, Optimal quantum cloning of orbital angular momentum photon qubits via hong-ou-mandel coalescence, Nat. Photonics **3**, 720 (2009).

[33] P. Y. Li, B. Wang, and X. D. Zhang, High-dimensional encoding based on classical nonseparability, Opt. Express **24**, 15143 (2016).